Unsteady Navier-Stokes Computations Past Oscillating Delta Wing at High Incidence

Osama A. Kandil* and H. Andrew Chuang†
Old Dominion University, Norfolk, Virginia 23529

The unsteady, compressible, thin-layer, Navier-Stokes equations, written in the moving frame of reference for the flow relative motion, are solved for the unsteady supersonic flow around a round-edged delta wing. For supersonic flow, a local conical flow solution has been obtained from the three-dimensional equations. Pseudo-time stepping is used for the steady flow problem; while time-accurate stepping is used for the unsteady flow problem. The computational scheme is an implicit, approximately factored, finite-volume scheme, which uses implicit and explicit dissipation terms. The scheme is verified for the steady flow solution. The scheme is then applied to a delta wing undergoing rolling oscillation at a reduced frequency of 1.337 with 15-deg maximum amplitude about a mean angle of attack of 10 deg for a Mach number of 2 and a Reynolds number of 0.5×10^6.

Introduction

THE literature on the computational solution and experimental data of unsteady vortex-dominated flows including shock waves around delta wings is unfortunately very limited. This is attributed to the complexity of the flow and its dependence on numerous variables and parameters. The unsteady flow is characterized by the existence of time-dependent primary, secondary, and trailing vortices, moving shock waves with time-dependent strengths, shock-vortex-core and shock-boundary-layer interactions, time-dependent vortex-core formation and breakdown, and wing aeroelastic deformations and structure instabilities.

Most of the existing unsteady computational schemes are based on the unsteady small disturbance (TSD) theory,[1,2] unsteady full potential (UFP) equation,[3-5] UTSD equation with nonisentropic flow corrections,[6] and UFP equation with nonisentropic flow corrections.[7] These schemes are restricted to attached flows only. For mildly separated flows, integral and finite-difference boundary-layer schemes have been coupled with potential flow schemes.[8,9]

The unsteady Euler equations adequately model shock waves and their motion, entropy increase across shocks, entropy gradient and vorticity production, and convection behind shocks, as can be seen from Crocco's theorem and the inviscid vorticity transport equation. Moreover, the computational solution of Euler equations adequately models separated flow from sharp edges.[10-12,17,18] For smooth-surface separation, round-edge separation, shock-induced separation, viscous diffusion and dissipation, vortex breakdown, flow transition and turbulence, viscous terms must be added to the Euler equations to recover the full Navier-Stokes equations or an approximate form of these equations.

Recently, successful time-accurate solutions of the unsteady Euler and Navier-Stokes equations have been presented for airfoils.[13-16] The only existing unsteady Euler solutions for vortex-dominated flows including shock waves are those of the rolling-oscillation of a sharp-edge delta wing in a locally conical supersonic flow around a mean angle of attack and a zero angle of attack, which were presented by the authors in Refs. 11 and 12. The authors derived the unsteady Euler equations for the flow relative motion in a general moving frame of reference, and the equations were solved by using an explicit, multistage time stepping, finite-volume scheme. Periodic solutions were achieved in the third cycle of rolling oscillation. Details of the surface pressure, crossflow velocity, and crossflow Mach contours were presented showing the primary-vortex and shock-wave formations and interaction. Secondary and tertiary vortices were not captured since Euler equations were used.

In Refs. 17 and 18, the authors presented the first successful time-accurate Euler-equations solution for a three-dimensional, sharp-edged delta wing undergoing pitching oscillation around the quarter-chord axis about a large mean angle of attack for low-speed flows. The problem was solved using an implicit, approximately factored, finite-volume scheme with added explicit and implicit artificial dissipation terms. The unsteady results were verified by comparisons with the corresponding computational results obtained from another code, known as CFL3D, which uses an implicit, flux-difference splitting, finite-volume scheme.[14]

In the present paper, the viscous effects are added to the unsteady Euler equations through the thin-layer, Navier-Stokes equations written in the moving frame of reference for the flow relative motion. The equations are solved using an implicit, approximately factored, finite-volume scheme for the steady and unsteady supersonic flow around a round-edged delta wing. The round-edged delta wing problem is a typical case where the Euler equations fail to produce a real flow solution.[10] Moreover, with the Navier-Stokes equations, secondary and tertiary vortices can be captured. Here, the application covers a delta wing undergoing rolling oscillation at a reduced frequency of 1.337 with 15-deg maximum amplitude about a mean angle of attack of 10 deg for a Mach number of 2. These are the same conditions as those of the Euler solution of Ref. 11 for a sharp-edged delta wing.

Formulation

In the absolute frame of reference, the unsteady, compressible Navier-Stokes equations in the conservation form are given by

$$\frac{\partial \rho}{\partial t} + \nabla \cdot (\rho \bar{V}) = 0 \tag{1}$$

$$\frac{\partial}{\partial t}(\rho \bar{V}) + \nabla \cdot (\rho \bar{V}\bar{V} + p\bar{I} - \bar{\tau}) = 0 \tag{2}$$

Received Jan. 9, 1989; revision received April 4, 1989.

*Eminent-Scholar Professor, Department of Mechanical Engineering and Mechanics. Associate Fellow AIAA.

†Visiting Assistant Professor, Department of Mechanical Engineering and Mechanics. Member AIAA.

$$\frac{\partial}{\partial t}(\rho e) + \nabla \cdot (\rho h \bar{V} - \bar{\tau} \cdot \bar{V} + \bar{q}) = 0 \tag{3}$$

$$p = (\gamma - 1)\left(\rho e - \frac{\rho}{2} V^2\right)$$

$$h = \frac{\gamma p}{\rho(\gamma - 1)} + \frac{V^2}{2} \tag{4}$$

$$\bar{\tau} = \frac{2M_\infty \mu}{Re}\left[\bar{D} - \frac{\bar{I}}{3} tr(\bar{D})\right], \qquad \bar{D} = \frac{1}{2}(\bar{V}\nabla + \nabla \bar{V}) \tag{5}$$

$$\bar{q} = -\frac{M_\infty \mu}{(\gamma - 1) PrRe} \nabla T \tag{6}$$

$$\mu = T^{3/2}\left(\frac{1 + C}{T + C}\right), \qquad C = 0.4317 \tag{7}$$

$$Re = \frac{\rho_\infty V_\infty \ell}{\mu_\infty}, \qquad Pr = 0.72, \qquad M_\infty = \frac{V_\infty}{a_\infty} \tag{8}$$

In Eqs. (1–8), ρ is the density, $\bar{V}$ the fluid velocity, p the pressure, e the total energy per unit mass, T the temperature, μ the viscosity, Re the freestream Reynolds number, Pr the Prandtl number, M_∞ the freestream Mach number, V_∞ the freestream velocity, and γ the ratio of specific heats. The characteristic parameters are ℓ, a_∞, ρ_∞, T_∞, and μ_∞, which are the root chord, freestream speed of sound, freestream density, freestream temperature, and freestream viscosity. The Sutherland's constant C is the ratio of 198.6 R/460 R.

To express Eqs. (1–3) in terms of a moving frame of reference, denoted by ($'$), we use the following relations of the substantial and local derivatives of a scalar a and a vector $\bar{A}$:

$$\frac{Da}{Dt} = \frac{D'a}{Dt'} \tag{9a}$$

$$\frac{\partial a}{\partial t} = \frac{\partial' a}{\partial t'} - \bar{V}_t \cdot \nabla a \tag{9b}$$

$$\frac{D\bar{A}}{Dt} = \frac{D'\bar{A}}{Dt'} + \bar{\omega} \times \bar{A} \tag{9c}$$

$$\frac{\partial \bar{A}}{\partial t} = \frac{\partial' \bar{A}}{\partial t'} - \bar{V}_t \cdot \nabla \bar{A} + \bar{\omega} \times \bar{A} \tag{9d}$$

where

$$\bar{V}_t = \bar{V} - \bar{V}_r = \bar{V}_0 + \bar{\omega} \times \bar{r} \tag{10}$$

In Eqs. (9) and (10), $\bar{V}_t$ is the transformation velocity from the absolute frame to the moving frame, $\bar{V}_r$ the relative fluid flow velocity, $\bar{V}_0$ the translation velocity of the moving frame, $\bar{\omega}$ the angular velocity of the moving frame, and $\bar{r}$ the position vector of a fluid particle with respect to the moving frame. With the transformation given in Eq. (9), and in terms of the Cartesian coordinates, Eqs. (1–5) become

$$\frac{\partial' \hat{q}_r}{\partial t'} + \frac{\partial}{\partial x}(\hat{E}_r - \hat{E}_{vr}) + \frac{\partial}{\partial y}(\hat{F}_r - \hat{F}_{vr}) + \frac{\partial}{\partial z}(\hat{G}_r - \hat{G}_{vr}) = \hat{S} \tag{11}$$

where

$$\hat{q}_r = [\rho, \rho u_r, \rho v_r, \rho w_r, \rho e_r]' \tag{12}$$

$$\hat{E}_r = [\rho u_r, \rho u_r^2 + p, \rho u_r v_r, \rho u_r w_r, \rho u_r h_r]' \tag{13}$$

$$\hat{F}_r = [\rho v_r, \rho u_r v_r, \rho v_r^2 + p, \rho v_r w_r, \rho v_r h_r]' \tag{14}$$

$$\hat{G}_r = [\rho w_r, \rho u_r w_r, \rho v_r w_r, \rho w_r^2 + p, \rho w_r h_r]' \tag{15}$$

$$\hat{E}_{vr} = [0, \tau_{r_{xx}}, \tau_{r_{xy}}, \tau_{r_{xz}}, u_r \tau_{r_{xx}} + v_r \tau_{r_{xy}} + w_r \tau_{r_{xz}} - q_x]' \tag{16}$$

$$\hat{F}_{vr} = [0, \tau_{r_{yx}}, \tau_{r_{yy}}, \tau_{r_{yz}}, u_r \tau_{r_{yx}} + v_r \tau_{r_{yy}} + w_r \tau_{r_{yz}} - q_y]' \tag{17}$$

$$\hat{G}_{vr} = [0, \tau_{r_{zx}}, \tau_{r_{zy}}, \tau_{r_{zz}}, u_r \tau_{r_{zx}} + v_r \tau_{r_{zy}} + w_r \tau_{r_{zz}} - q_z]' \tag{18}$$

$$\begin{aligned}\hat{S} = [0, &-\rho a_{t_x}, -\rho a_{t_y}, -\rho a_{t_z}, -\rho[\bar{V}_r \cdot \bar{a}_0 + (\bar{\omega} \times \bar{r}) \cdot \bar{a}_0 \\ &+ \bar{V}_0 \cdot (\bar{a}_t - \bar{\omega} \times \bar{V}_r) + \bar{V}_r \cdot (\dot{\bar{\omega}} \times \bar{r}) \\ &+ (\bar{\omega} \times \bar{r}) \cdot (\dot{\bar{\omega}} \times \bar{r})] + V_t \cdot (\bar{\tau}_t \cdot \nabla)]'\end{aligned} \tag{19}$$

$$p = (\gamma - 1)\rho\left(e_r + \frac{V_r^2}{2} + \frac{V_t^2}{2}\right) \tag{20}$$

$$h_r = \frac{\gamma p}{\rho(\gamma - 1)} + \frac{V_r^2}{2} - \frac{V_t^2}{2} \tag{21}$$

$$\bar{a}_t = \bar{a}_0 + \dot{\bar{\omega}} \times \bar{r} + 2\bar{\omega} \times \bar{V}_r + \bar{\omega} \times (\bar{\omega} \times \bar{r}) \tag{22}$$

where $\bar{a}_0$ is the translation acceleration of the moving frame.

$$\tau_{r_{mn}} = \frac{M_\infty \mu}{Re}\left(\frac{\partial u_{r_m}}{\partial X_n} + \frac{\partial u_{r_n}}{\partial X_m} - \frac{2}{3}\delta_{mn}\frac{\partial u_{r_p}}{\partial X_p}\right) \tag{23}$$

$$q_m = \frac{-M_\infty \mu}{(\gamma - 1) PrRe}\frac{\partial T}{\partial X_m} \tag{24}$$

$$\begin{aligned}\bar{V}_t \cdot \bar{\tau}_r \cdot \nabla &= u_{t_n}\frac{\partial \tau_{r_{mn}}}{\partial X_m} \\ &= \frac{M_\infty}{Re} u_{t_n}\frac{\partial}{\partial X_m}\left[\mu\left(\frac{\partial u_{r_m}}{\partial X_n} + \frac{\partial u_{r_n}}{\partial X_m} - \frac{2}{3}\delta_{mn}\frac{\partial u_{r_p}}{\partial X_p}\right)\right]\end{aligned} \tag{25}$$

In Eqs. (11–19), if $\bar{\tau}_r$ and $\bar{q}$ vanish in the Euler limit, we obtain the unsteady Euler equations in the moving frame of reference. In Eqs. (23) and (25), δ_{mn} is the Kronecker delta.

Computational Method

Since the equations are expressed in the moving frame of reference, the grid is carried with the moving frame. Hence, using the time-independent body conformed coordinates ξ, η, and ζ in the moving frame of reference given by

$$\xi = \zeta(x,y,z), \qquad \eta = \eta(x,y,z), \qquad \zeta = \zeta(x,y,z) \tag{26}$$

and using the thin-layer, Navier-Stokes approximation, i.e., keeping the viscous and heat transfer derivatives in the ζ direction (normal to the body) and neglecting the ξ and η derivatives of the viscous and heat transfer terms, Eq. (11) reduces to

$$\frac{\partial' Q_r}{\partial t'} + \frac{\partial E_r}{\partial \xi} + \frac{\partial F_r}{\partial \eta} + \frac{\partial}{\partial \zeta}(G_r - G_{vr}) = S \tag{27}$$

where

$$Q_r = J^{-1}\hat{q}_r \tag{28}$$

$$E_r = J^{-1}[\xi_x \hat{E}_r + \xi_y \hat{F}_r + \xi_z \hat{G}_r] \tag{29}$$

$$F_r = J^{-1}[\eta_x \hat{E}_r + \eta_y \hat{F}_r + \eta_z \hat{G}_r] \tag{30}$$

$$G_r = J^{-1}[\zeta_x \hat{E}_r + \zeta_y \hat{F}_r + \zeta_z \hat{G}_r] \tag{31}$$

$$G_{vr} = J^{-1}[\zeta_x \hat{E}_{vr} + \zeta_y \hat{F}_{vr} + \zeta_z \hat{G}_{vr}] \tag{32}$$

$$S = J^{-1}\hat{S} \tag{33}$$

Equation (27) is integrated over ξ, η, and ζ of the computational domain, and the divergence theorem is applied to the spatial derivative terms to obtain

$$\iiint_{\forall} \frac{\partial' Q_r}{\partial t'} \, d\forall + \iint_A E_r \, d\eta \, d\zeta + \iint_A F_r \, d\xi \, d\zeta + \iint_A (G_r - G_{vr}) \, d\xi \, d\eta = \iiint_{\forall} S \, d\forall \tag{34}$$

where $\forall$ is the domain of integration, and A is its boundary. Equation (34) is applied to each cell of the grid. The resulting equation for a cell with a centroidal point i,j,k is given by

$$\left(\frac{\partial' Q_r}{\partial t'}\right)_{i,j,k} = -[E_{r_{i+1/2,j,k}} - E_{r_{i-1/2,j,k}} + F_{r_{i,j+1/2,k}} - F_{r_{i,j-1/2,k}} + (G_r - G_{vr})_{i,j,k+1/2} - (G_r - G_{vr})_{i,j,k-1/2} - S_{i,j,k} - D_e(\hat{q}_{r_{i,j,k}})] = -W(\hat{q}_{r_{i,j,k}}) \tag{35}$$

where $W(\hat{q}_{r_{i,j,k}})$ is the spatial difference expression of the inviscid fluxes, viscous fluxes, source term, and explicit dissipation D_e. The expression of explicit dissipation is given in Ref. 12. The half integer subscripts refer to the cell interface. Using the Euler implicit method, the left-hand side of Eq. (35) is discretized using forward differencing for the time derivative and central differencing for the spatial derivatives. The resulting difference expression of Eq. (35) in the delta form is given by

$$\left(\frac{I}{J\,\Delta t'} + \delta_\xi A_r^n + \delta_\eta B_r^n + \delta_\zeta C_r^n - \delta_\zeta C_{vr}^n - \frac{H_r^n}{J}\right) \Delta\hat{q}_r^n = -W(\hat{q}_r^n) \tag{36}$$

where I is the identity matrix and δ the three-point, central-difference operator. The Jacobians A_r^n, B_r^n, C_r^n, C_{vr}^n, and H_r^n are given by

$$A_r^n = \frac{\partial E_r^n}{\partial \hat{q}_r}, \quad B_r^n = \frac{\partial F_r^n}{\partial \hat{q}_r}, \quad C_r^n = \frac{\partial G_r^n}{\partial \hat{q}_r}, \quad C_{vr}^n = \frac{\partial G_{vr}^n}{\partial \hat{q}_r}, \quad H_r^n = \frac{\partial \hat{S}^n}{\partial \hat{q}_r} \tag{37}$$

The left-hand side of Eq. (36) is approximately factored, and implicit dissipation operators ($D_{i\xi}$,$D_{i\eta}$,$D_{i\zeta}$) are added to obtain the scheme

$$\left[\frac{I}{J\,\Delta t'} + \delta_\xi A_r^n - D_{i\xi}\right]\left[\frac{I}{J\,\Delta t'} + \delta_\eta B_r^n - D_{i\eta}\right] \times \left[\frac{I}{J\,\Delta t'} + \delta_\zeta C_r^n - \delta_\zeta C_{vr}^n - \frac{H_r^n}{J} - D_{i\zeta}\right] \Delta\hat{q}_r^n = -\frac{1}{(J\,\Delta t')^2} W(\hat{q}_r^n) \tag{38}$$

The implicit dissipation operators have similar forms. In the ξ direction, the implicit dissipation operator is given by

$$D_{i\xi} = \varepsilon_m CFL(\Delta\nabla)_\xi \tag{39}$$

where ε_m is the implicit dissipation coefficient, CFL the Courant-Friedricks-Lewy number, and Δ and ∇ the forward and backward difference operators.

For the conical flow solution, Eq. (38) is solved in three planes using the three-dimensional program. Since the absolute motion of the unsteady conical flow is assumed to be locally conical, the absolute conservative components of the flow vector ρ, ρu, ρv, ρw, ρe are forced to be constant on three planes. In terms of the flow relative motion these conditions are given by

$$\rho_{2\pm1} = \rho_2 \tag{40}$$

$$\rho\bar{V}_{r_{2\pm1}} = \rho\bar{V}_{r_2} + \rho\bar{\omega} \times (\bar{r}_2 - \bar{r}_{2\pm1}) \tag{41}$$

$$\rho e_{r_{2\pm1}} = \rho e_{r_2} + (\rho\bar{V}_{r_2} + \rho\bar{\omega} \times \bar{r}_2) \cdot [\bar{\omega} \times (\bar{r}_2 - \bar{r}_{2\pm1})] \tag{42}$$

where the subscript 2 refers to the middle plane, and the subscript 2 ± 1 refers to the first and third planes.

The computational domain is extended to a size such that the bow shock formed outside the wing is captured as a part of the solution. Outside of the bow shock, the flow conditions are those of the freestream conditions.

The solid surface boundary condition is obtained from the normal momentum equation as

$$\frac{\partial P}{\partial n} = -\rho\hat{e}_n \cdot \bar{a}_t \tag{43}$$

where $\hat{e}_n$ is the unit outward normal to the wing surface. Obviously for the steady flow, Eq. (43) reduces to $\partial P/\partial n = 0$. The adiabatic boundary condition is taken as the temperature condition.

For the unsteady flow, the initial conditions for the flow relative motion are obtained by subtracting the terms due to the impulsively started motion of the moving frame from the absolute steady solution

$$\rho\bar{V}_r = \rho\bar{V} - \rho\bar{\omega} \times \bar{r} \tag{44}$$

$$\rho e_r = \rho e - \rho\bar{V} \cdot (\bar{\omega} \times \bar{r}) \tag{45}$$

For steady-flow problems, local-time stepping is used; while for the unsteady-flow problem, global minimum time stepping is used for the time-accurate solution.

Computational Results

A round-edged delta wing of a sweep-back angle β of 70 deg, a half-vertex angle δ of 1.5 deg at a mean angle of attack α_m of 10 deg and in a freestream Mach number of 2, and a Reynolds number of 0.5×10^6 is considered for the computational application. The body conformed grid is generated by using a modified Joukowski transformation[11] of 190×90 cells (around and normal to the wing) for the steady symmetric flow and 380×90 cells for the unsteady asymmetric flow. The CRAY XMP computer of the Numerical Aerodynamic Simulation (NAS) facilities at NASA Ames Research Center is used to produce the present results.

Steady Laminar Viscous Flow

Figure 1 shows the results for the steady-flow problem. In this figure, we show the surface pressure, the crossflow velocity, the total-pressure-loss contours, and a blowup of the crossflow velocity near the leading edge. On the surface-pressure figure, we also show the results of Thomas and Newsome[19] using the implicit, flux-vector splitting, finite-volume scheme with a grid of 151×75. Both results are in excellent agreement. The crossflow velocity and its blowup and the total-pressure-loss figures show the primary and secondary vortices and a tertiary vortex as well. The crossflow velocity shows a shock above the primary vortex near its inner boundary and a small shock under the primary vortex, inboard of the secondary vortex. It should be noticed that the peak suction pressure of the surface-pressure figure shows two peaks corresponding to the primary and secondary vortices. This case took 4000 time steps to reduce the residual error by six orders of magnitude. The CPU time per grid point per time step is about 25×10^{-6} s.

The results of the steady-flow case serve as the initial conditions for the unsteady-flow case as follows.

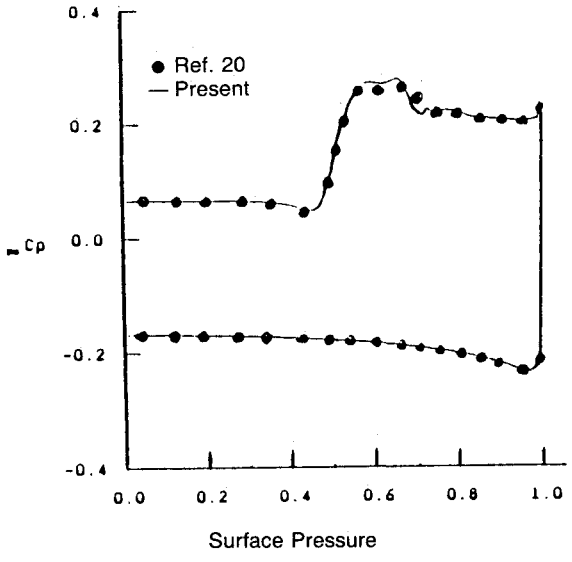

Surface Pressure

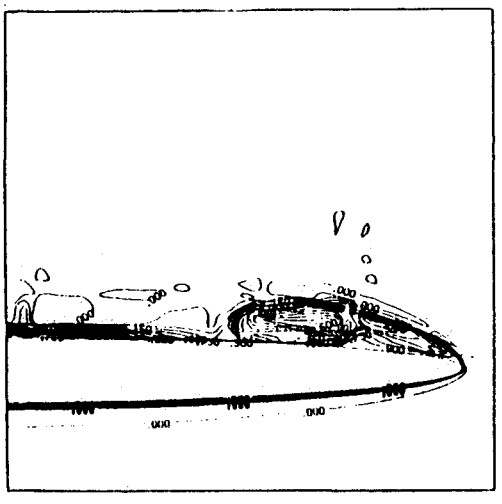

Total-Pressure Loss

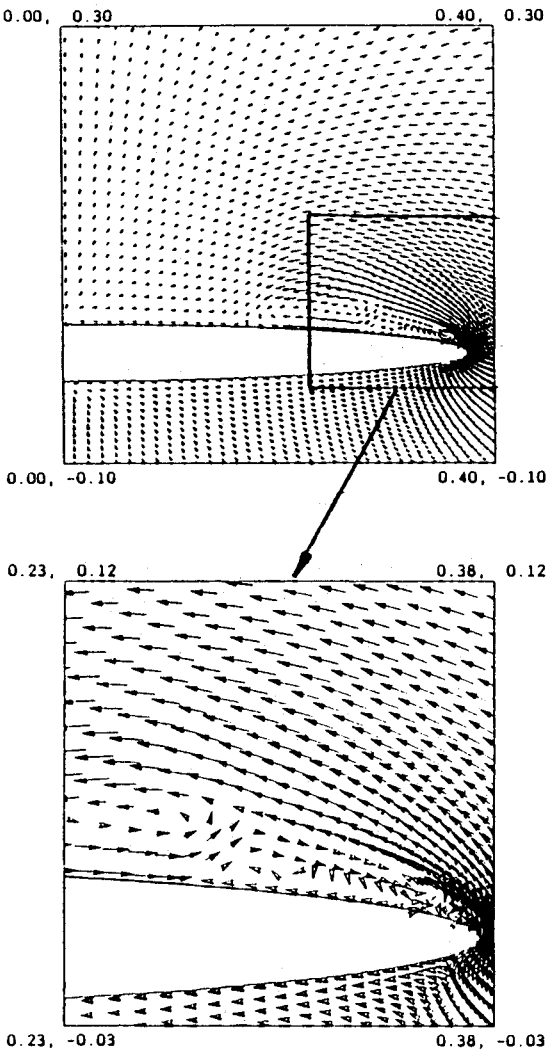

Cross-Flow Velocity

Fig. 1 Steady flow solution, $\alpha = 10$ deg, $M_\infty = 2$, $AR = 1.5$, $\delta = 1.5$ deg, $Re = 0.5 \times 10^6$.

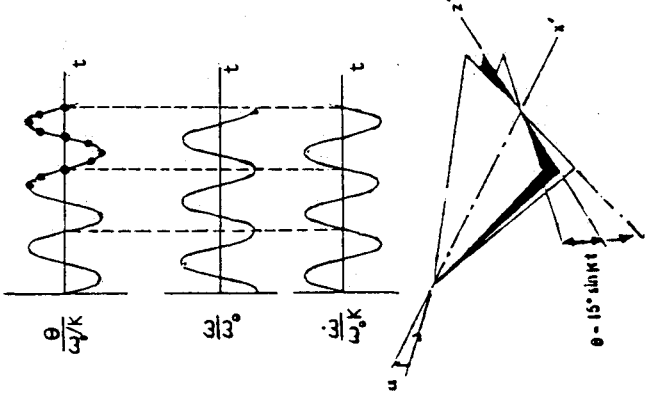

Fig. 2 Rolling oscillation motion, $k = 1.337$, $\theta_{max} = 15$ deg.

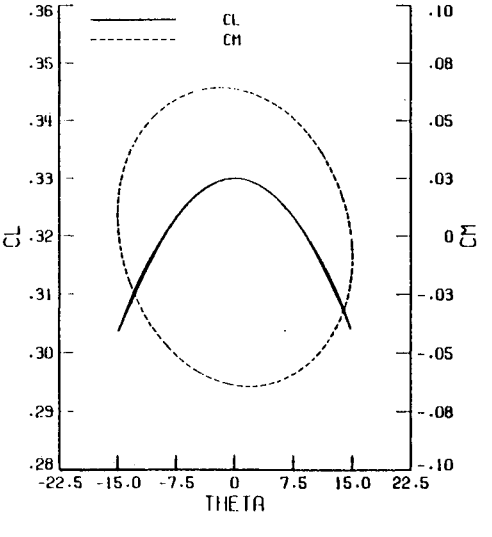

Fig. 3 Lift and rolling-moment coefficients for periodic solution.

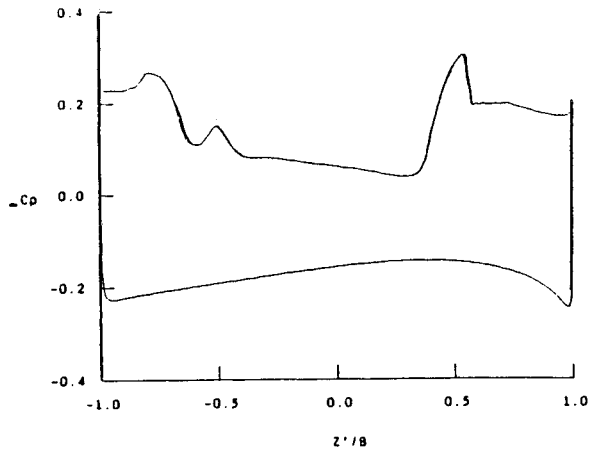

Surface Pressure

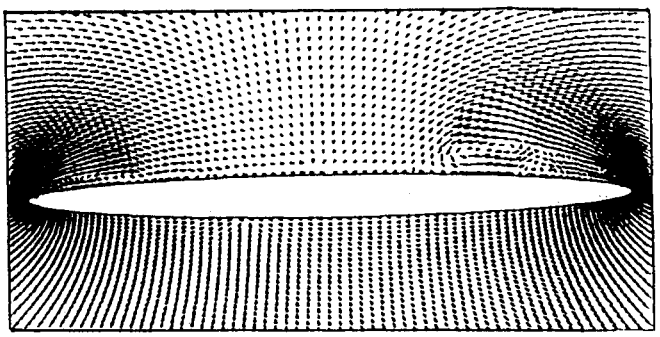

Cross-Flow Velocity

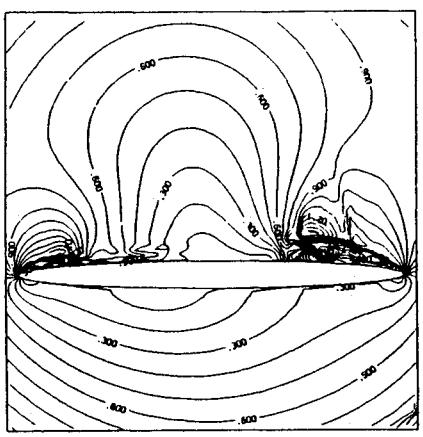

Cross-Flow Mach

Fig. 4 Flow characteristics, $t = 8.225$, $n = 3290$, $\theta = 15$ deg ↓.

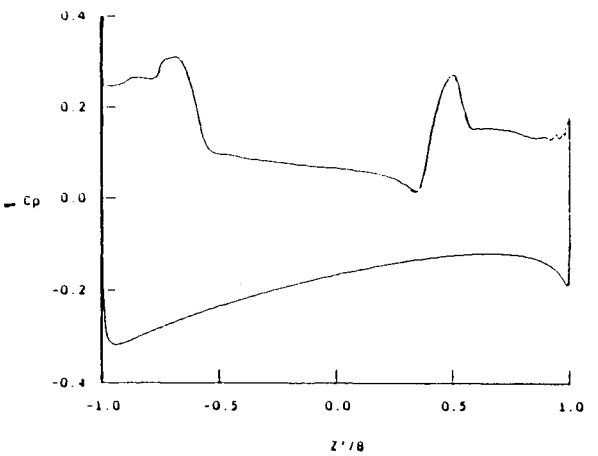

Surface Pressure

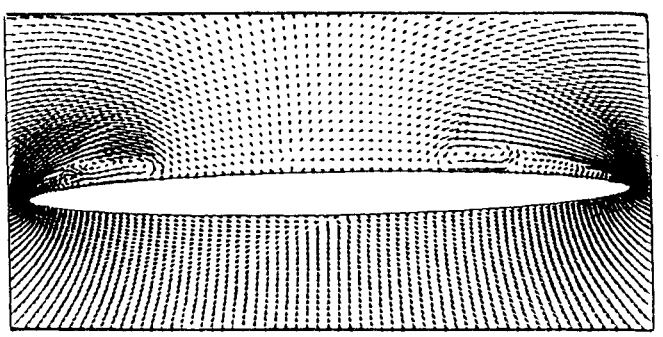

Cross-Flow Velocity

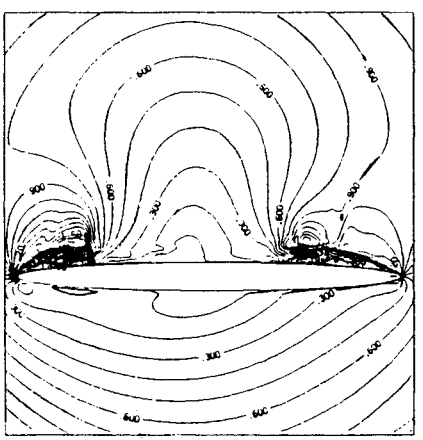

Cross-Flow Mach

Fig. 5 Flow characteristics, $t = 8.8125$, $n = 3525$, $\theta = 10.607$ deg ↓.

Unsteady Laminar-Viscous Flow for the Rolling Oscillation

The wing is given a rolling sinusoidal oscillation of $\bar{\omega}$ and θ given by

$$\bar{\omega} = -\omega_0 \cos kt \hat{e}_x, \qquad \theta = -\theta_{\max} \sin kt \tag{46}$$

where $\theta_{\max} = \omega_0/k$ is the maximum amplitude of roll angle, k is the dimensionless reduced frequency ($k = k^* \ell / U_\infty$, where k^* is the dimensional frequency and ℓ is the root chord), and $\hat{e}_x$ is a unit vector parallel to the x axis of the moving frame of reference. In the present case, $\theta_{\max} = \pi/12 = 15$ deg, $k = 1.337$, and $\omega = 0.35$. The corresponding period of oscillation is 4.7. The average value of the minimum global time step is 2.5×10^{-3}, and hence each cycle of oscillation takes 1880 time steps. Figure 2 shows the rolling oscillation motion.

Figure 3 shows the computed lift coefficient C_L and rolling-moment coefficient C_M vs the roll angle θ during the periodic response, which has been achieved during the third cycle of oscillation. The wing starts the rolling oscillation at $\theta = 0$ rolling in the counterclockwise (CCW) direction relative to an observer looking in the upstream direction ($-\hat{e}_x$). The rolling-moment coefficient shows a typical hysteresis response; while the lift coefficient shows a slight hysteresis response. Moreover, the lift-coefficient curve is symmetric, as expected, at about the $\theta = 0$-deg position since the response of the lift coefficient during the first half of the cycle on the left side is

a mirror image to that during the second half of the cycle on the right side.

Next, we show details of the flow characteristics during the last quarter of the second cycle and the first quarter of the third cycle. These are shown in Figs. 4–8 covering the time step number range $n = 3290–4230$, which corresponds to the time range $t = 8.225–10.575$. In each figure, we show the surface pressure, the crossflow velocity, and the crossflow Mach contours.

In Fig. 4, we show the results at $n = 3290$ or $t = 8.255$ where the roll angle $\theta = +15$ deg and the wing is rolling in the CCW direction. On the wing suction side, the surface pressure shows two peaks on the left side corresponding to the diminishing secondary and primary vortices. The right side shows one suction peak corresponding to a strong primary vortex and a strong shock beneath the vortex as seen in the crossflow Mach contours figure. The crossflow velocity shows the picture very clearly.

In Fig. 5, we show the results at $n = 3525$ or $t = 8.8125$ where the roll angle $\theta = +10.605$ deg and the wing is rolling in the CCW direction. On the wing suction side, the surface pressure shows a strong suction peak along with a vortex and a weak secondary vortex. On the right side, a strong suction peak (smaller than the one of Fig. 4) is seen corresponding to the primary vortex and a shock beneath the vortex. The crossflow velocity and the crossflow Mach contours clearly show the details of the flow.

In Fig. 6, $n = 3760$ or $t = 9.4$ where the roll angle $\theta = 0$ and the wing is still rolling in the CCW direction. At this instant, the wing section is horizontal, and the wing has completed

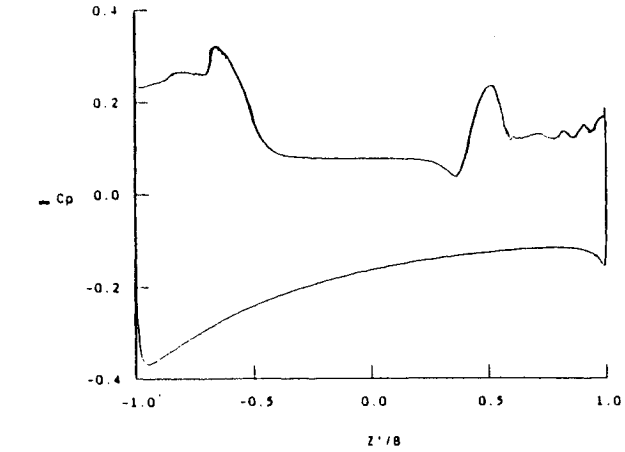

Surface Pressure

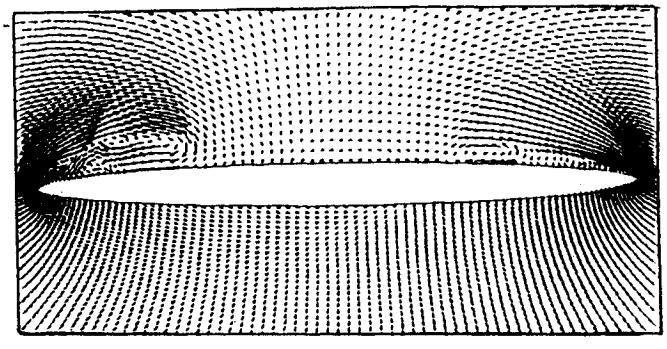

Cross-Flow Velocity

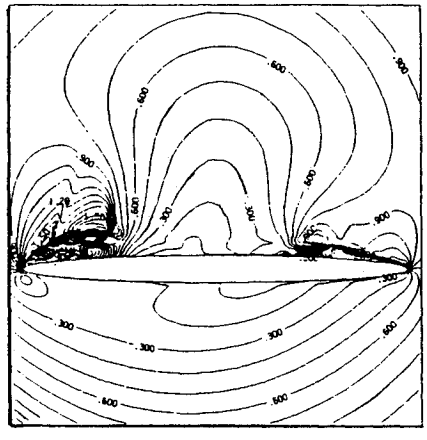

Cross-Flow Mach

Fig. 6 Flow characteristics, $t = 9.4$, $n = 3760$, $\theta = 0$ deg ↓.

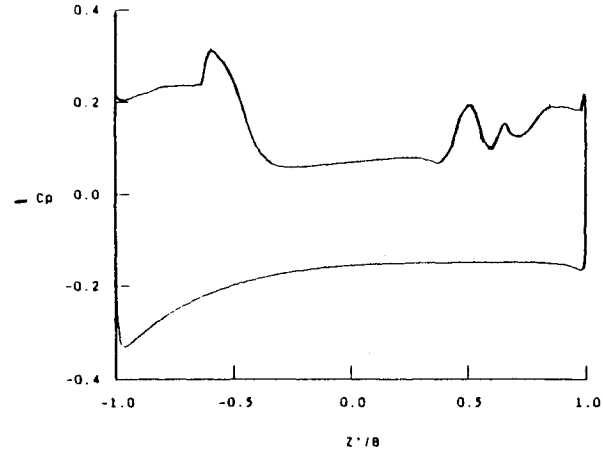

Surface Pressure

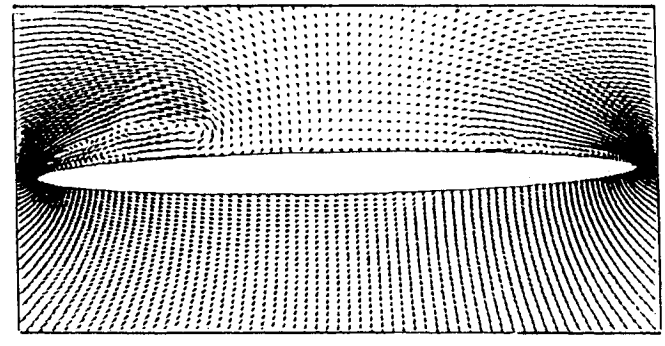

Cross-Flow Velocity

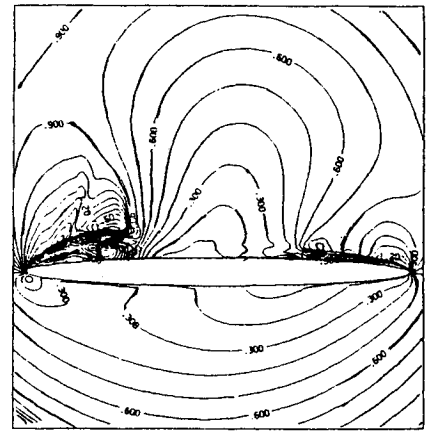

Cross-Flow Mach

Fig. 7 Flow characteristics, $t = 9.9875$, $n = 3995$, $\theta = -10.607$ deg ↓.

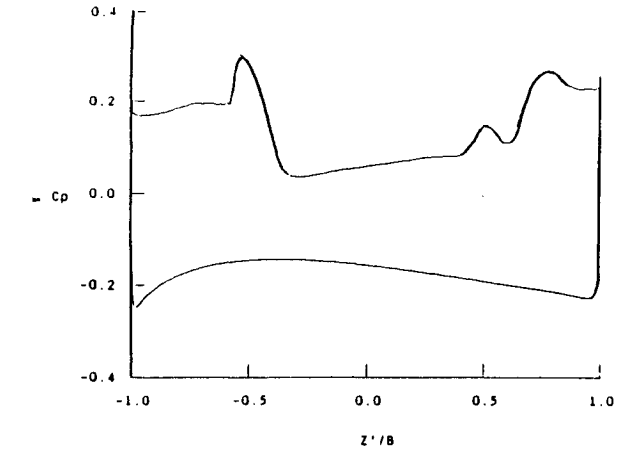

Surface Pressure

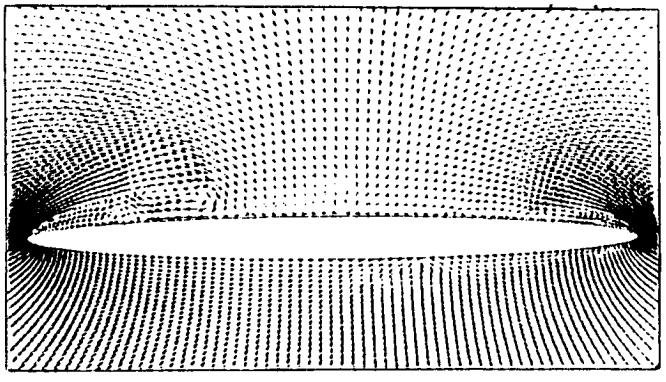

Cross-Flow Velocity

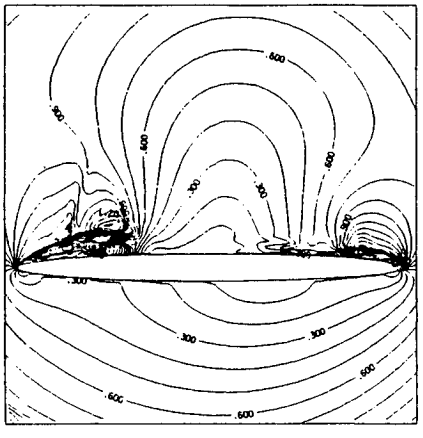

Cross-Flow Mach

Fig. 8 Flow characteristics, $t = 10.575$, $n = 4230$, $\theta = -15$ deg ↑.

two cycles of oscillation. On the suction side, the surface pressure on the left side shows a stronger suction peak (than that of Fig. 5) with a smaller peak to the left. The larger peak on the left side is moving inboard to the right, and a strong shock is formed under the primary vortex. On the right side, the peak suction pressure is decreasing, and the primary and secondary vortices are splitting and diffusing.

In Fig. 7, $n = 3995$ or $t = 9.9875$ where the roll angle $\theta = -10.605$ deg, and the wing is still rolling in the CCW direction. On the suction side, the surface pressure on the left side shows an increasing suction peak, which is still moving inboard to the right with a stronger shock under the primary vortex and less pronounced pressure peak of the secondary vortex. On the right side, the primary and secondary vortices are splitting, diffusing, and diminishing.

In Fig. 8, $n = 4230$ or $t = 10.575$ where the roll angle $\theta = -15$ deg, and the wing is reversing the rolling motion to the clockwise (CW) direction. By comparing the results at this instant to those of Fig. 4 ($\theta = +15$ deg), one notices that the flow response at the present instant on the left and right sides is the same as that of Fig. 4 on the right and left sides, respectively. Hence, periodic response of the flow has been achieved. The conference paper[20] shows additional responses during the third cycle of oscillation.

Concluding Remarks

The unsteady compressible, thin-layer, Navier-Stokes equations have been developed in the moving frame of reference for the flow relative motion. The resulting equations are solved using the implicit, approximately factored, finite-volume scheme for the steady and unsteady supersonic flow around a round-edged delta wings. The round-edged delta wing flow problem is a typical case where the Euler equations fail to produce a unique flow solution. The steady-flow results have been compared with those of the implicit flux-vector splitting, finite-volume scheme, and they are in excellent agreement. The present scheme has also been applied to a round-edged delta wing undergoing rolling oscillation around the wing axis about a large mean angle of attack. The time history of the lift and rolling-moment coefficients has been presented. The computed flow characteristics (surface pressure, crossflow velocity, and crossflow Mach contours) have been presented and described to study the behavior of the primary vortex, secondary vortex, and shock waves including their interaction.

Acknowledgment

This research work has been supported by the NASA Langley Research Center under Grant NAG-1-648.

References

[1]Ballhaus, W. F., and Goorjian, P. M., "Implicit Finite-Difference Computations of Unsteady Transonic Flows about Airfoils," *AIAA Journal*, Vol. 15, Dec. 1977, pp. 1728–1735.

[2]Edwards, J. W., Bland, S. R., and Seidel, D. A., "Experience with Transonic Unsteady Aerodynamic Calculations," NASA TM-86278, 1984.

[3]Chipman, R., and Jameson, A., "Full Conservative Numerical Solutions for Unsteady Irrotational Transonic Flow about Airfoils," AIAA Paper 79-1555, July 1979.

[4]Goorjian, P. M., "Implicit Computations of Unsteady Transonic Flow Governed by the Full Potential Equation in Conservation Form," AIAA Paper 80-0150, Jan. 1980.

[5]Ruo, S. Y., Malone, J. B., and Sankar, L. N., "Steady and Unsteady Full Potential Calculations for High and Low Aspect Ratio Supercritical Wings," AIAA Paper 86-0122, Jan. 1986.

[6]Batina, J. T., "Unsteady Transonic Small-Disturbance Theory Including Entropy and Vorticity Effects," AIAA Paper 88-2278-CP, April 1988.

[7]Whitlow, W., Jr., "Application of a Nonisentropic Full Potential Method to AGARD Standard Airfoils," AIAA Paper 88-0710, Jan. 1988.

[8]Howlett, J. T., and Bland, S. R., "Calculation of Viscous Effects on Transonic Flow for Oscillating Airfoils and Comparisons with Experiment," NASA TP-2731, Sept. 1987.

[9]Weinberg, B. C., and Shamroth, S. J., "Three-Dimensional Unsteady Viscous Flow Analysis Over Airfoil Sections," NASA CR-172368, 1984.

[10]Kandil, O. A., and Chuang, H. A., "Influence of Numerical Dissipation on Computational Euler Equations for Vortex-Dominated Flows," *AIAA Journal*, Vol. 25, Nov. 1987, pp. 1426–1434.

[11]Kandil, O. A., and Chuang, H. A., "Computation of Steady and Unsteady Vortex-Dominated Flows," *AIAA Journal*, Vol. 26, May 1988, pp. 524–531.

[12]Kandil, O. A., and Chuang, H. A., "Unsteady Vortex-Dominated Flows Around Maneuvering Wings Over a Wide Range of Mach

Numbers," AIAA Paper 88-0317, Jan. 1988.

[13]Kandil, O. A., and Chuang, H. A., "Unsteady Transonic Airfoil Computation Using Implicit Euler Scheme on Body-Fixed Grid," *AIAA Journal*, Vol. 27, Aug. 1989, pp. 1031–1037.

[14]Anderson, W. K., Thomas, J. L., and Rumsey, C. L., "Extension and Applications of Flux-Vector Splitting to Unsteady Calculations on Dynamic Meshes," AIAA Paper 87-1152-CP, 1987.

[15]Visbal, M. R., and Shang, J. S., "Numerical Investigation of the Flow Structure Around a Rapidly Pitching Airfoils," AIAA Paper 87-1424, June 1987.

[16]Rumsey, C. L., and Anderson, W. K., "Some Numerical and Physical Aspects of Unsteady Navier-Stokes Computations Over Airfoils Using Dynamic Meshes," AIAA Paper 88-0329, Jan. 1988.

[17]Kandil, O. A., and Chuang, H. A., "Prediction of Unsteady Loads on Manuevering Delta Wings Using Time-Accurate Euler Schemes," AIAA Paper 88-2280-CP, April 1988, pp. 504–512.

[18]Kandil, O. A., and Chuang, H. A., "Unsteady Delta-Wing Flow Computation Using an Implicit Factored Euler Scheme," AIAA/ASME/SIAM/APS First National Fluid Dynamics Congress, AIAA, Washington, DC, July 1988, pp. 248–255.

[19]Thomas, J. L., and Newsome, R. W., "Navier-Stokes Computations of Lee-Side Flows Over Delta Wings," AIAA Paper 86-1049, May 1986.

[20]Kandil, O. A., and Chuang, H. A., "Unsteady Navier-Stokes Computations Past Oscillating Delta Wing at High Incidence," AIAA Paper 89-0081, Jan. 1989.